RESEARCH ARTICLE

Reconstruction of Fan Beam X-Ray Fluorescence Computed Tomography Based on Parallel Hole Collimator via Total Variation and Ordered Subsets

SHANGHAI JIANG[1,2,3]**, LE CHEN**[3]**, JIE ZHONG**[3]**, LI AI**[1]**, HUA YANG**[2]**, AND HONG LU**[1]

[1]Department of Radiology, Seventh People's Hospital of Chongqing, Central Hospital Affiliated to Chongqing University of Technology, Chongqing 400054, China
[2]Department of Medical Imaging, Chongqing Traditional Chinese Medicine Hospital, Chongqing 400021, China
[3]Chongqing Key Laboratory of Optical Fiber Sensor and Photoelectric Detection, Chongqing University of Technology, Chongqing 400054, China

Corresponding authors: Hua Yang (13527547568@163.com) and Hong Lu (471739847@qq.com)

ABSTRACT In this paper, an Ordered Subsets Expectation Maximization (OSEM) reconstruction algorithm based on Total Variation (TV) constraint was applied for sparse reconstruction of X-ray fluorescence CT. First, the Geant4 Monte Carlo code was used to simulate the imaging process of fan beam X-ray fluorescence CT imaging system based on parallel hole collimator. Then, the reconstructed image quality of the proposed algorithm with varying numbers of projections was evaluated using RMSE and CNR. Finally, the relationship between the number of subsets of the algorithm and the quality of the reconstructed image and the reconstruction time was explored. The results demonstrated that, compared with the conventional OSEM algorithm, the proposed OSEM algorithm based on Total Variation constraint has higher quality of reconstructed images at different projection numbers, and the reconstruction time of the algorithm decreases with the increase of subset, which achieves the purpose of improving the quality of the reconstructed image and reducing the reconstruction time when sparse reconstruction.

INDEX TERMS X-ray fluorescence CT, image reconstruction, Monte Carlo simulation, sparse projection, total variation.

I. INTRODUCTION

X-ray fluorescence computed tomography (XFCT) is a molecular imaging method that can simultaneously obtain the distribution and content of elements in the sample in a non-invasive and non-destructive way [1]. The principle is to use external X-rays to excite high Z elements inside the sample to produce radiation fluorescence, and the distribution and content of elements in the sample can be reconstructed from the projection data by reconstruction algorithm. As a result, XFCT has a broad application prospect in the early

The associate editor coordinating the review of this manuscript and approving it for publication was Yi Zhang.

diagnosis of cancer and other fields [2], [3]. However, the X-rays used in X-ray fluorescence CT are prone to cause serious damage to human body at high doses. Therefore, how to maintain the quality of the reconstructed images while reducing the number of projection (that is, reducing the X-ray dose) is a key technical problem to be solved urgently in the clinical application of X-ray fluorescence CT.

At present, the algorithm based on Total Variation (TV) constraint has been widely used in X-ray computed tomography (X-CT) image reconstruction [4], [5], [6], [7], [8], [9], [10]. Researchers have optimized the X-CT algorithm based on Total Variation constraint and proposed some new reconstruction algorithms. For example, Zhang et al. [11] proposed

a directional total variation (DTV) algorithm, which can accurately recover the phantom from data generated within the significantly reduced angular range, and can significantly reduce the artifacts observed in the reconstruction of existing algorithms. Xi et al. [12] proposed a high order total variation (HOTV) reconstruction algorithm. Compared with the traditional TV algorithm, the proposed algorithm can effectively suppress the staircase effect and improve the reconstruction accuracy. Gong et al. [13] proposed a prior image induced relative total variation (piiRTV) reconstruction model for limited angle CT. Their experimental results show that this model can suppress noise and reduce most shadow artifacts through the adaptive weight determined by the prior structure. The Ordered Subset Algorithm was initially used to accelerate X-ray CT reconstruction and was later applied to validate X-ray fluorescence CT in different imaging geometries [14], [15], [16], [17], [18], [19], [20], [21]. Although some researchers have applied Total Variation constraint to X-ray fluorescence CT image reconstruction [22], [23], its application to XFCT system with parallel hole collimation has not been reported. Therefore, in this study, we proposed an X-ray fluorescence reconstruction method based on ordered subsets and total variation. Projection data were generated using Geant4 simulations to verify the effectiveness of the algorithm. Our results may provide new evidence for sparse projection reconstruction for this imaging geometry.

II. MATERIALS AND METHODS
A. THEORETICAL BASIS OF FAN BEAM XFCT
The schematic diagram of the fan beam XFCT system is shown in Figure 1, which is mainly composed of X-ray source, parallel hole collimator, phantom and fluorescent array detector. As shown in the Figure 1, the acquisition of projection data can be divided into two steps: 1) The interaction between incident X-ray and phantom at point B generates radiant fluorescence; 2) The radiation fluorescence is detected and recorded by the array detector. A single X-ray is used as an example to describe the general process: the X-rays emitted by the X-ray tube are attenuated and absorbed by the AB path segment in the phantom, and the high Z elements in the phantom are excited by X-ray at point B to produce radiation fluorescence X-rays; After being attenuated and absorbed by the BC path segment in the phantom, the excited fluorescent X-rays are detected and recorded by the array detector [15]. Therefore, the final fluorescence intensity collected by the detection unit P is:

$$I_F = \int_\alpha \left\{ \left[I_0 \exp\left(-\int_A^B \mu_I dl \right) \right] \mu_{ph} \omega \rho \right.$$
$$\left. \left[\int_\Omega \exp\left(-\int_B^C \mu_F dl \right) d\Omega \right] \right\} d\alpha' \quad (1)$$

where I_0 is the initial intensity of the incident X-ray, μ_I is the absorption coefficient at the energy of the incident X-ray, μ_{ph} is the photoelectric absorption coefficient, ω is

the fluorescence yield, ρ is the element mass concentration at point B, Ω is the solid angle from the detection unit P to point B, μ_F is the absorption coefficient at the energy of the radiation fluorescence, and α is the fan beam angle of the X-ray source, α' is the integration variable.

For the phantom with regular shape and uniform distribution of elements, the projection data can be directly calculated by equation (1). In reality, the shape of the phantom is usually irregular, and the distribution of elements in the phantom is not uniform. Therefore, in order to effectively utilize the above methods to obtain the projection data, the XFCT projection process is generally discretized: the reconstructed image is divided into the form of grids in two-dimensional space, and each grid is called one pixel. Assuming that the distribution of elements within each pixel is uniform, the ith projection is expressed as:

$$p_i = \sum_j a_{ij} x_j \quad (2)$$

where a_{ij} represents the contribution value of the jth pixel to the ith projection, x_j represents the jth pixel of the reconstructed image X, and p_i represents the number of fluorescent photons recorded by the ith detection unit.
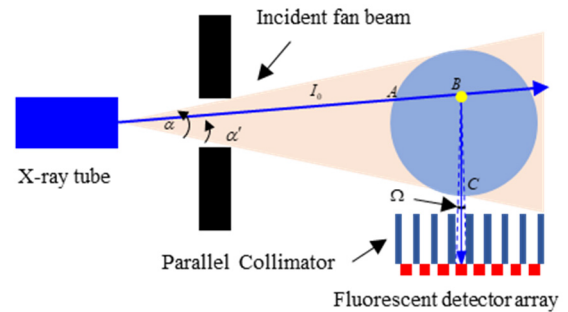
FIGURE 1. Schematic diagram of fan-beam XFCT system.

B. OSEM-BASED TV RECONSTRUCTION ALGORITHM
To reduce the reconstruction time and effectively improve the computational efficiency, OSEM algorithm was used for reconstruction in this paper. As an EM algorithm based on OS method, the principle of OSEM algorithm is to divide the projection data of X-ray fluorescence CT into m ordered subsets, then the standard EM algorithm is used to maximize the likelihood function for each subset in turn, and the reconstruction result is taken as the initial value of the next subset. Therefore, OSEM algorithm can be described as follows:

$$x_j^{(k+1)} = \frac{x_j^{(k)}}{\sum_{i \in S_m} a_{ij}} \sum_{i \in S_m} a_{ij} \frac{p_i}{\sum_j a_{ij} x_j^{(k)}} \quad (3)$$

where S_m is the ith subset of projection. It can be seen from the above that OSEM algorithm is actually an algorithm that applies EM algorithm to each subset. During each reconstruction, the projection data in the subset will correct each

pixel at the same time, and the reconstructed image will be updated once. After one OSEM iteration is completed, the reconstructed image will be updated m times, which makes the more subsets of the OSEM algorithm, the shorter the reconstruction time. Equation (2) is expressed in matrix form, the reconstruction problem of fan beam XFCT can be described as follows:

$$AX = P \qquad (4)$$

where A is the projection matrix, X is the reconstructed image, P is the projection data. When the projection matrix A and projection data P are known, the reconstructed image X can be obtained by equation (4).Actually in the reconstruction process, due to the ill-condition of the projection matrix, there are errors between the reconstructed image and the real image, and it is almost impossible to accurately obtain the real image from equation (4). In order to make the reconstructed image as close as possible to the real image, TV was used to optimize the reconstructed image in this paper, and the optimization problem obtained is as follows:

$$\min|X|_{TV}, \ s.t. \ |P - AX| < e, X \geqslant 0 \qquad (5)$$

where $|X|_{TV}$ is the total variation of the reconstructed image X which is defined as follows:

$$|X|_{TV} = \sum_{s,t} \sqrt{\left(X_{s,t} - X_{s-1,t}\right)^2 + \left(X_{s,t} - X_{s,t-1}\right)^2} \qquad (6)$$

Equation (5) is solved by gradient descent method [17]. The solution steps are as follows:

①Initialize the reconstructed image $X^{(k=0)} = 0$, where k is the number of current iterations;

②OSEM algorithm was used to complete one iteration and the reconstructed image $X^{(k+1)}$ is obtained;

③$X_{POCS}^{(k+1)}$ is obtained by setting the negative value in $X^{(k+1)}$ to 0;

$$X_{POCS}^{(k+1)} = \begin{cases} X^{(k+1)}, & X^{(k+1)} \geqslant 0 \\ 0, & X^{(k+1)} < 0 \end{cases} \qquad (7)$$

④Initialize $X_{n=0}^{(k+1)} = X_{POCS}^{(k+1)}$;

⑤Calculate incremental factor d_{k+1}:

$$d_{k+1} = \left\| X^{(k)} - X_{n=0}^{(k+1)} \right\|_2 \qquad (8)$$

⑥Calculate the total variational gradient v and the gradient direction Iv, as shown in the equations at the bottom of the page, where ε is a small parameter to avoid instability induced by zero denominator.

⑦Iteratively correct the image $X_n^{(k+1)}$ until $n = N$, otherwise repeat steps ⑥-⑦, where N is the total number of iterations in the process of minimizing TV.

$$X_{n+1}^{(k+1)} = X_n^{(k+1)} - \lambda d_{k+1} Iv \qquad (11)$$

⑧Iteratively correct the image X^{k+1} until $k = K$, otherwise repeat steps ②-⑧. Where K is the total number of iterations of the algorithm.

To sum up, the algorithm flow of OSEM-TV is shown in Figure 2.

C. XFCT IMAGING SYSTEM

The schematic diagram of Geant4 simulation setup is seen in Figure3(a), which includes X-ray tube source, phantom, parallel collimator, fluorescent detector array and CCD array. The phantom shown in Fig.3(b) is a PMMA cylinder with a diameter of 50mm, containing eight small holes with a diameter of 10mm, in which neodymium nitrate solutions with concentrations of 2%, 4%, 6% and 8% are embedded, respectively. The brass collimator consists of 64 square holes with an area of 1mm × mm, a hole depth of 8mm, and a hole spacing of 1mm. The detector consists of 254 detection units with the size of 0.5mm ×0.5 mm, the energy spectrum resolution of 0.1 keV. The distances from the center of the phantom to the X-ray source and the collimation hole are 37 cm and 3.6 cm, respectively. During the simulation, the particle transport process, includes photoelectric effect, Compton scattering and Rayleigh scattering, is defined by G4EmLivermorePhysics.list.

$$
\begin{aligned}
v(s, t) &= \frac{\partial \left| X_n^{(k+1)} \right|_{TV}}{\partial X_n^{(k+1)}(s, t)} \\
&\approx \frac{\left(X_n^{(k+1)}(s, t) - X_n^{(k+1)}(s-1, t)\right) + \left(X_n^{(k+1)}(s, t) - X_n^{(k+1)}(s, t-1)\right)}{\sqrt{\varepsilon + \left(X_n^{(k+1)}(s, t) - X_n^{(k+1)}(s-1, t)\right)^2 + \left(X_n^{(k+1)}(s, t) - X_n^{(k+1)}(s, t-1)\right)^2}} \\
&\quad - \frac{\left(X_n^{(k+1)}(s+1, t) - X_n^{(k+1)}(s, t)\right)}{\sqrt{\varepsilon + \left(X_n^{(k+1)}(s+1, t) - X_n^{(k+1)}(s, t)\right)^2 + \left(X_n^{(k+1)}(s+1, t) - X_n^{(k+1)}(s+1, t-1)\right)^2}} \\
&\quad - \frac{\left(X_n^{(k+1)}(s, t+1) - X_n^{(k+1)}(s, t)\right)}{\sqrt{\varepsilon + \left(X_n^{(k+1)}(s, t+1) - X_n^{(k+1)}(s, t)\right)^2 + \left(X_n^{(k+1)}(s, t+1) - X_n^{(k+1)}(s-1, t+1)\right)^2}} \qquad (9)
\end{aligned}
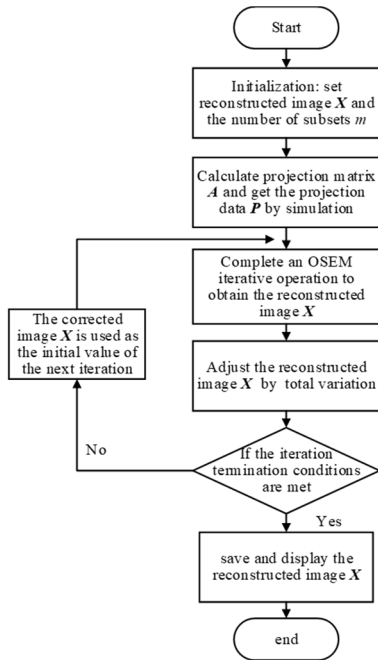$$

$$Iv = \frac{v}{\|v\|_2} \qquad (10)$$

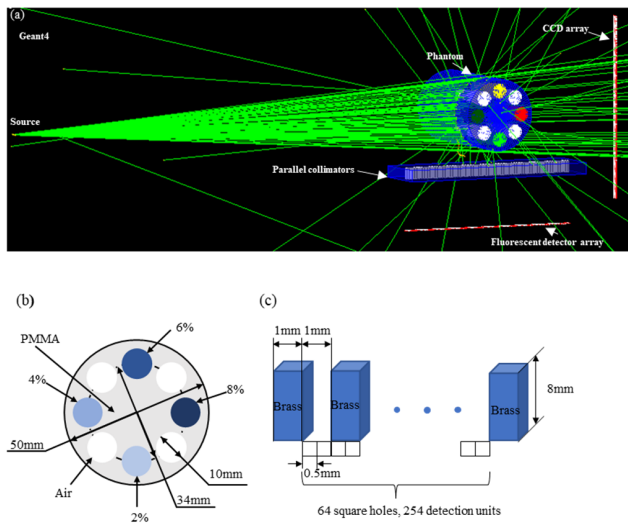**FIGURE 2.** Flow chart of OSEM-TV algorithm.

FIGURE 3. The Geant4 simulation of fan beam XFCT. (a) The simulation of the XFCT system based on Geant4; (b) Phantom parameters; (c) Array detector parameters.

D. XFCT IMAGING SIMULATION

In order to improve the efficiency of Geant4 simulation, the energy spectrum of the incident X-ray source was calculated using SpekCalc software [24], as shown in Figure 4 (a). The X-ray source, featuring tungsten as the target material, operates at 70 kVp with a beryllium filter of 0.8 mm, an aluminum filter of 1.0 mm, and a copper filter of 0.4 mm. According to the energy spectrum distribution of the incident X-ray source, 1 billion photons were randomly emitted from the X-ray source point at each projection angle during the

simulation, and the direction of the photons were randomly sampled within the fan angle. The radiation fluorescence generated by the element excitation in the phantom and partially scattered photons were collimated through the hole and recorded by the detection unit. During the simulation, full scan imaging was performed at one degree interval. When the sampling angle was 90 degrees, the energy spectrum recorded by the 90th detection unit was shown in figure 4(b). The fluorescent photons were superimposed on the scattering spectrum, and the fluorescence energy of $K_{\alpha1}$ and $K_{\alpha2}$ were 37.5kev and 37.0kev, respectively. To extract a more accurate number of X-ray fluorescence photons, cubic polynomial fitting was used in this paper to calculate the number of scattered photons, as shown in Figure 4(c). The selected energy range for this fitting was 31.8-42.2kev. Therefore, the number of fluorescent photons can be calculated by the following formula [25]:

$$N_{\text{fluo}} = N_{total} - N_{\text{scatter}} \tag{12}$$

where N_{fluo} is the number of fluorescence photons, N_{total} is the total number of photons in the range of 31.8kev to 42.2kev, and N_{scatter} is the number of scattered photons.

Since the hole spacing is 1 mm, there are only 128 detection units that can collect fluorescent photons. The number of fluorescence photons recorded in four adjacent detection units were merged, and the merged result was used as one projection. The X-ray fluorescence sinogram obtained by arranging the projection data according to the projection angle is presented in Figure 5.

III. RESULTS

A. RECONSTRUCTION IMAGE EVALUATION

In this paper, RMSE and CNR were used to evaluate the quality of the reconstructed image [26]. The Root Mean Square Error (RMSE) was used to evaluate the similarity between the reconstructed image and the real image. The smaller the value, the higher the similarity. The Contrast to noise ratio (CNR) was defined to evaluate the image quality. Only when the CNR value of the image is greater than or equal to 4, the target region and background region can be clearly distinguished. Their expressions are as follows:

$$RMSE = \sqrt{\frac{\sum_{i=1}^{M}\sum_{j=1}^{N}(A1(i,j) - A(i,j))^2}{M \times N}} \tag{13}$$

$$CNR = \frac{|\overline{\Psi}_{ROI} - \overline{\Psi}_{BKG}|}{\sigma_{BKG}} \tag{14}$$

where ROI and BKG are the target and background regions in the sample. $\overline{\Psi}_{ROI}$ and $\overline{\Psi}_{BKG}$ are the mean pixel values of the corresponding regions, respectively. σ_{BKG} is the standard deviation of the background region. $A1$ is the reconstructed image. A is the real image. $M \times N$ is the size of the image.
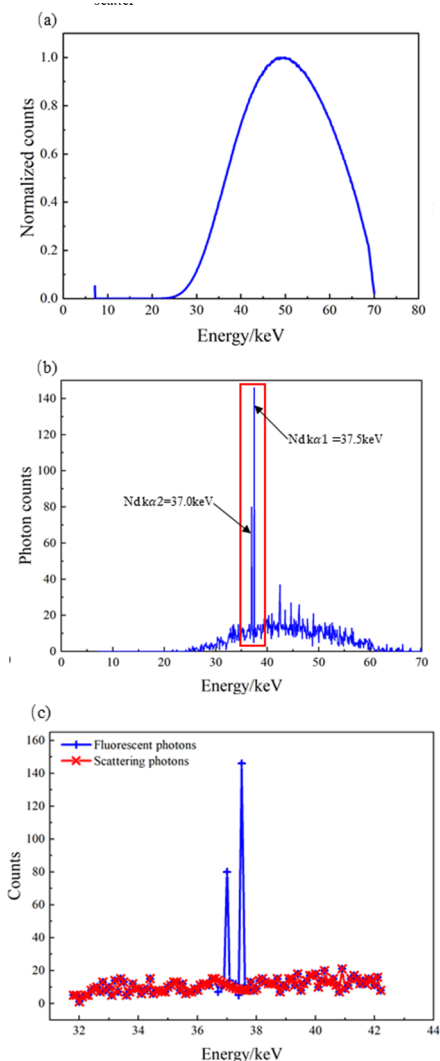
FIGURE 4. Acquisition of fluorescent photons. (a) The energy spectrum of incident X-ray source; (b) X-ray fluorescence spectrum of the 90th detection unit; (c) Scattering photon distribution fitting of the 90th detection unit.
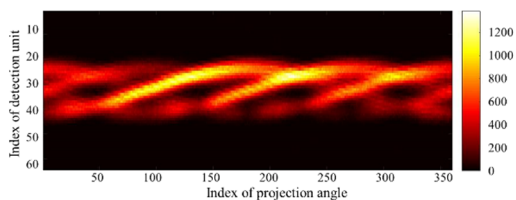

FIGURE 5. X-ray fluorescence sinogram.

B. IMAGE RECONSTRUCTION AND ANALYSIS

OSEM algorithm and OSEM-TV algorithm were used for reconstruction in this work, respectively. During the reconstruction process, the adjustment factor λ was set to 0.03, the number of iterations was set to 100, and the number of subsets was set to 5 according to experience. The reconstructed images of the two algorithms at different projection numbers (30, 40, 45, 60, 90, 120, 180, 360) are shown in Figure 6.

Figure 6(a)-(h) shows the reconstructed XFCT images by the OSEM algorithm, and Figure 6(i)-(p) shows the reconstructed XFCT images by the OSEM-TV algorithm. We magnified the same region of interest in each reconstructed image to compare the reconstruction effects of the two algorithms. Obviously, as the number of projections increases, the image quality for both algorithms improve significantly. However, for any given projection number, the OSEM-TV algorithm consistently delivers superior image quality compared to the OSEM algorithm. This indicates that the OSEM-TV algorithm not only enhances image reconstruction quality but also allows for larger projection intervals, effectively reducing projection time while achieving high-quality reconstruction under sparse projection conditions.
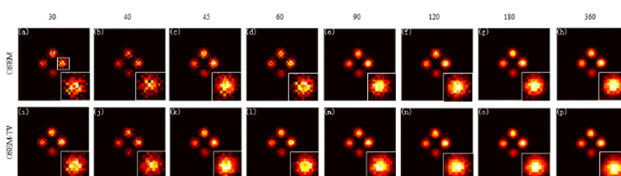
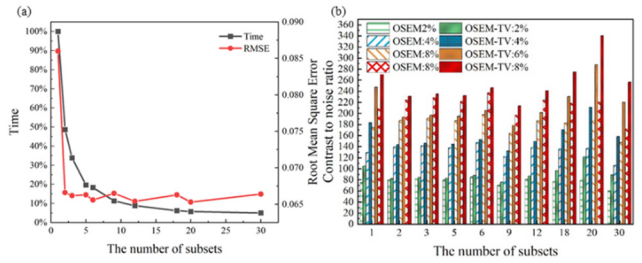**FIGURE 6.** Reconstructed images of two algorithms under different numbers of projections.

In order to further quantitatively analyze the superiority of the OSEM-TV algorithm and the influence of the number of projections on the quality of the reconstructed image, the normalized RMSE and CNR values of the two algorithms at different projection numbers were calculated, respectively. The results are shown in Figure 7. With the increase of the number of projections, the reconstructed image quality of the two algorithms is improved. When the number of projections is the same, the RMSE value of the image reconstructed by OSEM-TV algorithm is smaller than that of the image reconstructed by OSEM algorithm, and the CNR value is larger than that of the image reconstructed by OSEM algorithm. Obviously, compared with the conventional OSEM algorithm, no matter whether the projection interval is large or small, OSEM-TV algorithm can better suppress the root mean square error of the reconstructed image, and the contrast to noise ratio between the target region and the background region of the reconstructed image of the OSEM-TV algorithm is higher. Therefore, two conclusions can be drawn: 1) when the number of projections is small, the recon-structed image quality of the two reconstruction algorithms is poor; 2) the proposed algorithm can effectively improve the quality of the reconstructed image, and the purpose of improving the reconstructed image quality in sparse projection is achieved.

Figure 8 (a) shows the relationship between the number of subsets and the normalized RMSE value and the reconstruction time when OSEM-TV algorithm was used for reconstruction. Theoretically, as the number of subsets increases, the reconstruction time of the OSEM-TV algorithm gradually decreases, while the quality of the reconstructed
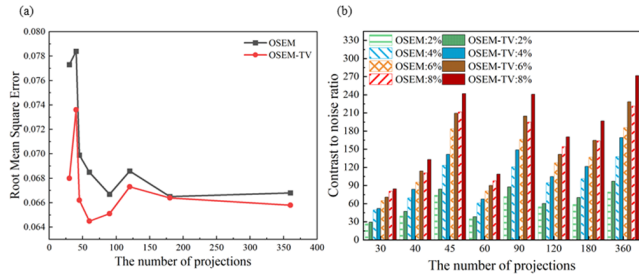
FIGURE 7. The evaluation parameters of the two algorithms under different numbers of projections. (a) The normalized RMSE of reconstructed images of the two algorithms under different numbers of projections; (b) The CNR of reconstructed images of the two algorithms under different numbers of projections.

FIGURE 8. The evaluation parameters under different numbers of subsets. (a) The normalized RMSE and reconstruction time of reconstructed images of OSEM-TV algorithms under different numbers of subsets; (b) The CNR of reconstructed images of the two algorithms under different numbers of subsets.

image remains unchanged. However, in the reconstruction process, the number of subsets is one of the factors affecting the accuracy of the reconstructed image, as shown in Figure 8 (a). With the increase of the number of subsets, the reconstruction time of OSEM-TV algorithm gradually decreases, but the normalized RMSE value of the reconstructed image of OSEM-TV algorithm fluctuates within a certain range. In particular, when the number of subsets is 2, the image reconstruction time is decreased to 48.6%, the normalized RMSE value of the reconstructed image is significantly reduced; when the number of subsets is 20, the change of image reconstruction time tends to be flat. In summary, it can be considered that when the projection interval is 1° and the number of iterations is 360, the optimal number of subsets reconstructed by OSEM-TV algorithm is 20. It means that when the number of subsets is 20, only 18 iterations are required to achieve the same effect as 360 iterations without dividing subsets, effectively accelerating the convergence of iterations and reducing reconstruction time. In this experiment, without dividing subsets, the reconstruction time was approximately 4 minutes (Intel(R) Core (TM) i5-12600K CPU @ 3.69GHz) for a reconstructed image size of 128×128. For such a reconstruction size, dividing subsets is generally unnecessary. However, when reconstructing larger images, this approach can significantly reduce the reconstruction time. To analyze the influence of the number of subsets on the quality of the reconstructed image, the CNR values of the reconstructed images of the two algorithms were calculated respectively when the number of subsets was different (1, 2, 3, 5, 6, 9, 12, 18, 20, 30) and the number of iterations (360) and projection interval (1°) were the same, as shown in Figure 8(b): with the increase of the number of subsets, when the number of subsets is the same, the CNR value of the image reconstructed by OSEM algorithm is greater than that of the image reconstructed by OSEM algorithm. This shows that, no matter the number of subsets is large or small, the contrast to noise ratio between the target region and the background region of the reconstructed image of the OSEM-TV algorithm is larger, and the quality of the reconstructed image is better.

IV. DISCUSSION

In this study, we proposed a reconstruction method for fan beam X-ray fluorescence computed tomography based on parallel hole collimator that combines Ordered Subsets (OS) with Total Variation (TV). Projection data generated through Geant4 simulations were used to preliminarily validate the feasibility of the method for sparse projection reconstruction. Compared with conventional algorithms, the proposed method effectively reduces noise, suppresses artifacts, and accelerates iterative convergence.

While reconstruction formulations for different imaging geometries can be uniformly represented by Equation (4), the corresponding weight matrices A vary depending on the imaging geometry [1], [20], [22], [23], [27], [28]. Feng et al. [3], [29] proposed a multi-pinhole collimated L-shell fluorescence CT system based on Total Variation (TV). Shi et al. [30] proposed a quantitative X-ray fluorescence CT method based on the L_1−norm and Total Variation (TV). Some researchers have also applied Total Variation (TV) to novel imaging geometries to verify the feasibility of the method. The method proposed in this study aims to provide a complementary option for XFCT imaging. To obtain projection data, we adopted a phantom similar to those used in prior studies [19], [27], consisting of a PMMA cylinder containing cylindrical regions of interest. The phantom is computationally efficient to model in Geant4 due to its simplicity, enabling faster simulations. Additionally, it is straightforward to fabricate for experimental validation in our future studies. This work represents an initial exploration of the algorithm's effectiveness using simulation. Future studies will focus on theoretical analysis of its convergence properties and further validation with experimental data to provide a more comprehensive assessment of the method's applicability and reliability.

V. CONCLUSION

The feasibility of OSEM-TV for fan-beam XFCT in sparse reconstruction was verified in this work. During the reconstruction, the projection interval is an important factor affecting the image quality of XFCT reconstruction. When the projection interval increase, OSEM-TV algorithm can

effectively improve the quality of XFCT reconstructed images. The results demonstrated that, compared with the OSEM algorithm, the OSEM-TV algorithm can better suppress the root mean square error, effectively improve the quality and shorten the reconstruction time. Therefore, the superiority of the OSEM-TV algorithm in XFCT reconstruction over the OSEM algorithm in sparse projection, which has positive significance for the process of promoting the application of X-ray fluorescence CT to clinical medicine, and lays a theoretical foundation for further improving the quality of reconstructed images in sparse reconstruction and accelerating the reconstruction speed.

REFERENCES

[1] M. Ahmad, G. Pratx, M. Bazalova, and L. Xing, "X-ray luminescence and X-ray fluorescence computed tomography: New molecular imaging modalities," *IEEE Access*, vol. 2, pp. 1051–1061, 2014.

[2] J. Chen, S. Zhang, W. Fang, L. I. Liang, and T. University, "The latest development of X-ray fluorescence computed tomography," *Chin. J. Stereology Image Anal.*, vol. 23, no. 1, pp. 102–116, 2018.

[3] J. Guo, P. Feng, L. Deng, Y. Luo, P. He, and B. Wei, "Optimization of detection angle for pinhole X-ray fluorescence computed tomography," *Acta Optica Sinica*, vol. 40, no. 1, pp. 237–245, 2020.

[4] S. Sarkar, P. Wahi, and P. Munshi, "Total variation (TV) ℓ1 norm minimization based limited data X-ray CT image reconstruction," *Res. Nondestruct. Eval.*, vol. 31, no. 3, pp. 164–186, May 2020.

[5] D. Thanh, P. Surya, and L. M. Hieu, "A review on CT and X-ray images denoising methods," *Informatica*, vol. 43, no. 2, pp. 151–159, Jun. 2019.

[6] X. Luo, W. Yu, and C. Wang, "An image reconstruction method based on total variation and wavelet tight frame for limited-angle CT," *IEEE Access*, vol. 6, pp. 1461–1470, 2018.

[7] L. Lei, W. Lin-Yuan, X. Xiao-Qi, H. Yu, Y. Bin, and B. Shang-Lian, "X-ray CT energy spectrum estimation algorithm based on weighted TV normalization," *Spectrosc. Spectral Anal.*, vol. 37, no. 7, pp. 2230–2236, 2017.

[8] S. Niu, Y. Gao, Z. Bian, J. Huang, W. Chen, G. Yu, Z. Liang, and J. Ma, "Sparse-view X-ray CT reconstruction via total generalized variation regularization," *Phys. Med. Biol.*, vol. 59, no. 12, pp. 2997–3017, Jun. 2014, doi: 10.1088/0031-9155/59/12/2997.

[9] Y. Liu, Z. Liang, J. Ma, H. Lu, K. Wang, H. Zhang, and W. Moore, "Total variation-Stokes strategy for sparse-view X-ray CT image reconstruction," *IEEE Trans. Med. Imag.*, vol. 33, no. 3, pp. 749–763, Mar. 2014.

[10] Z. Qu, X. Yan, J. Pan, and P. Chen, "Sparse view CT image reconstruction based on total variation and wavelet frame regularization," *IEEE Access*, vol. 8, pp. 57400–57413, 2020.

[11] Z. Zhang, B. Chen, D. Xia, E. Y. Sidky, and X. Pan, "Directional-TV algorithm for image reconstruction from limited-angular-range data," *Med. Image Anal.*, vol. 70, May 2021, Art. no. 102030.

[12] Y. Xi, Z. Qiao, W. Wang, and L. Niu, "Study of CT image reconstruction algorithm based on high order total variation," *Optik*, vol. 204, Feb. 2020, Art. no. 163814.

[13] C. Gong, L. Zeng, and C. Wang, "Image reconstruction model for limited-angle CT based on prior image induced relative total variation," *Appl. Math. Model.*, vol. 74, pp. 586–605, Oct. 2019.

[14] H. M. Hudson and R. S. Larkin, "Accelerated image reconstruction using ordered subsets of projection data," *IEEE Trans. Med. Imag.*, vol. 13, no. 4, pp. 601–609, Dec. 1994, doi: 10.1109/42.363108.

[15] T. Yuasa, M. Akiba, T. Takeda, M. Kazama, A. Hoshino, Y. Watanabe, K. Hyodo, F. A. Dilmanian, T. Akatsuka, and Y. Itai, "Reconstruction method for fluorescent X-ray computed tomography by least-squares method using singular value decomposition," *IEEE Trans. Nucl. Sci.*, vol. 44, no. 1, pp. 54–62, Feb. 1997.

[16] F. J. Beekman and C. Kamphuis, "Ordered subset reconstruction for X-ray CT," *Phys. Med. Biol.*, vol. 46, no. 7, pp. 1835–1844, Jul. 2001.

[17] E. Y. Sidky, C.-M. Kao, and X. Pan, "Accurate image reconstruction from few-views and limited-angle data in divergent-beam CT," *J. X-ray Sci. Technol.*, vol. 14, no. 2, pp. 119–139, Jan. 2006.

[18] Q. Yang, B. Deng, W. Lv, F. Shen, R. Chen, Y. Wang, G. Du, F. Yan, T. Xiao, and H. Xu, "Fast and accurate X-ray fluorescence computed tomography imaging with the ordered-subsets expectation maximization algorithm," *J. Synchrotron Radiat.*, vol. 19, no. 2, pp. 210–215, Mar. 2012.

[19] B. Deng, G. Du, G. Zhou, Y. Wang, Y. Ren, R. Chen, P. Sun, H. Xie, and T. Xiao, "3D elemental sensitive imaging by full-field XFCT," *Analyst*, vol. 140, no. 10, pp. 3521–3525, 2015.

[20] L. Deng, S. Yasar, M. F. Ahmed, S. Jayarathna, P. Feng, B. Wei, S. Vedantham, A. Karellas, and S. H. Cho, "Investigation of transmission computed tomography (CT) image quality and X-ray dose achievable from an experimental dual-mode benchtop X-ray fluorescence CT and transmission CT system," *J. X-ray Sci. Technol.*, vol. 27, no. 3, pp. 431–442, Jul. 2019.

[21] H. Moktan, M. F. Ahmed, S. Jayarathna, L. Deng, and S. H. Cho, "Monte Carlo study of X-ray detection configurations for benchtop X-ray fluorescence computed tomography of gold nanoparticle-loaded objects," *Phys. Med. Biol.*, vol. 65, no. 17, Aug. 2020, Art. no. 175010.

[22] S. Zhang, L. Li, and Z. Chen, "Scattering noise model enhanced EM-TV algorithm for benchtop X-ray fluorescence computed tomography image reconstruction," *IEEE Access*, vol. 7, pp. 113589–113595, 2019.

[23] S. Zhang, L. Li, J. Chen, Z. Chen, W. Zhang, and H. Lu, "Quantitative imaging of Gd nanoparticles in mice using benchtop cone-beam X-ray fluorescence computed tomography system," *Int. J. Mol. Sci.*, vol. 20, no. 9, p. 2315, May 2019, doi: 10.3390/ijms20092315.

[24] G. Poludniowski, G. Landry, F. DeBlois, P. M. Evans, and F. Verhaegen, "SpekCalc: A program to calculate photon spectra from tungsten anode X-ray tubes," *Phys. Med. Biol.*, vol. 54, no. 19, pp. 433–438, Oct. 2009, doi: 10.1088/0031-9155/54/19/n01.

[25] S.-K. Cheong, B. L. Jones, A. K. Siddiqi, F. Liu, N. Manohar, and S. H. Cho, "X-ray fluorescence computed tomography (XFCT) imaging of gold nanoparticle-loaded objects using 110 kVp X-rays," *Phys. Med. Biol.*, vol. 55, no. 3, pp. 647–662, Feb. 2010, doi: 10.1088/0031-9155/55/3/007.

[26] D. Vernekohl, M. Ahmad, G. Chinn, and L. Xing, "Feasibility study of Compton cameras for X-ray fluorescence computed tomography with humans," *Phys. Med. Biol.*, vol. 61, no. 24, pp. 8521–8540, Dec. 2016.

[27] S. Yang, S. Jiang, S. Shi, X. Hu, and M. Zhao, "Numerical and Monte Carlo simulation for polychromatic L-shell X-ray fluorescence computed tomography based on pinhole collimator with sheet-beam geometry," in *Proc. MDPI*, Dec. 2022, vol. 9, no. 12, p. 928.

[28] Y. Chen, M. Du, G. Zhang, J. Zhang, K. Li, L. Su, F. Zhao, H. Yi, and X. Cao, "Sparse reconstruction based on dictionary learning and group structure strategy for cone-beam X-ray luminescence computed tomography," *Opt. Exp.*, vol. 31, no. 15, pp. 24845–24861, 2023.

[29] Y. Luo, P. Feng, J. Guo, R. Zhao, P. He, and B. Wei, "Simulation research of multi-pinhole collimated L-shell XFCT imaging system," *IEEE Access*, vol. 8, pp. 180273–180279, 2020, doi: 10.1109/ACCESS.2020.3028066.

[30] J. Shi, B. Granger, K. Xu, and Y. Yang, "Quantitative X-ray fluorescence imaging of gold nanoparticles using joint L1 and total variation regularized reconstruction," *Quant. Imag. Med. Surgery*, vol. 10, no. 1, pp. 184–196, Jan. 2020.

SHANGHAI JIANG received the Ph.D. degree in optical engineering from Chongqing University, in 2017. He is currently a Researcher with Chongqing Key Laboratory of Optical Fiber Sensor and Photoelectric Detection, Chongqing University of Technology. He is also conducting postdoctoral research in medical imaging with the Central Hospital Affiliated to Chongqing University of Technology and Chongqing Traditional Chinese Medicine Hospital. His research interests include X-ray fluorescence CT simulation and reconstruction, multiphoton fluorescence imaging, and medical image processing.

LE CHEN received the B.S. degree in optoelectronic information science and engineering from Chongqing University of Technology, where he is currently pursuing the master's degree in optical engineering with Chongqing Key Laboratory of Optical Fiber Sensor and Photoelectric Detection. His research interest includes medical image processing.

JIE ZHONG is currently pursuing the master's degree in optical engineering with the Key Laboratory of Optoelectronic Testing, Chongqing University of Technology. His research interests include artificial intelligence and photoelectric image processing.

LI AI received the bachelor's degree in radiology from Soochow University, in 2007, and the master's degree in pharmacy from Chongqing University of Technology, in 2023. She was with Yueyang Second People's Hospital, Hunan, from 2007 to 2012. She has been with Chongqing Seventh People's Hospital, since 2012. Since 2017, her primary research focus has been on the molecular mechanisms of brain edema and fMRI and targeted therapies for brain edema.
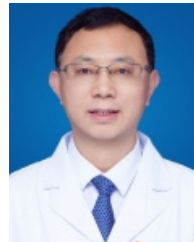
HUA YANG received the degree from the Medical Imaging Program, North Sichuan Medical College, in 2003, and the Ph.D. degree from Third Military Medical University, in 2013. He is a Chief Physician, a Professor, and the Doctoral/Postdoctoral Supervisor. His research interests include low-dose imaging techniques, CTA imaging technology, MRI molecular imaging, and integrative imaging combining Chinese and Western medicine.

HONG LU received the Ph.D. degree in neuroimaging from Chongqing Medical University. He completed his postdoctoral research in medical imaging with Zhejiang University. Over the course of 38 years, he has worked in imaging diagnosis, research, teaching, and management with the Imaging Center, Daping Hospital, Third Military Medical University; and the Radiology Department, Haikou Hospital, Xiangya School of Medicine, Central South University. Currently, he is with the Central Hospital Affiliated to Chongqing University of Technology. He is a Chief Physician, a Professor, and the Doctoral/Postdoctoral Supervisor. His research interests include molecular mechanisms of brain edema and fMRI, imaging diagnosis of gastrointestinal tumors, AI and medical imaging, and image processing.

• • •